Correlation of Local Structure and Diffusion Pathways in the Modulated Anisotropic Oxide Ion Conductor CeNbO$_{4.25}$

Stevin S. Pramana,[†] Tom Baikie,*[,‡] Tao An,[§] Matthew G. Tucker,[∥,⊥] Ji Wu,[†] Martin K. Schreyer,[#] Fengxia Wei,[◇] Ryan D. Bayliss,[†,△] Christian L. Kloc,[§] Timothy J. White,[§] Andrew P. Horsfield,[†] and Stephen J. Skinner*[,†]

[†]Department of Materials, Imperial College London, Exhibition Road, London SW7 2AZ, United Kingdom

[‡]Energy Research Institute at NTU, Research Technoplaza and [§]Division of Materials Science and Engineering, Nanyang Technological University, Nanyang Drive, Singapore, Singapore

[∥]ISIS Facility, Rutherford Appleton Laboratory, Didcot OX11 0QX, United Kingdom

[⊥]Diamond Light Source, Chilton, Oxfordshire, OX11 0DE, United Kingdom

[#]Institute of Chemical and Engineering Sciences, 1 Pesek Road, Jurong Island, Singapore

[◇]Institute of Materials Research and Engineering, 3 Research Link, Singapore, Singapore

S *Supporting Information*

ABSTRACT: CeNbO$_{4.25}$ is reported to exhibit fast oxygen ion diffusion at moderate temperatures, making this the prototype of a new class of ion conductor with applications in a range of energy generation and storage devices. To date, the mechanism by which this ion transport is achieved has remained obscure, in part due to the long-range commensurately modulated structural motif. Here we show that CeNbO$_{4.25}$ forms with a unit cell ~12 times larger than the stoichiometric tetragonal parent phase of CeNbO$_4$ as a result of the helical ordering of Ce^{3+} and Ce^{4+} ions along z. Interstitial oxygen ion incorporation leads to a cooperative displacement of the surrounding oxygen species, creating interlayer "NbO$_6$" connectivity by extending the oxygen coordination number

to 7 and 8. Molecular dynamic simulations suggest that fast ion migration occurs predominantly within the xz plane. It is concluded that the oxide ion diffuses anisotropically, with the major migration mechanism being intralayer; however, when obstructed, oxygen can readily move to an adjacent layer along y via alternate lower energy barrier pathways.
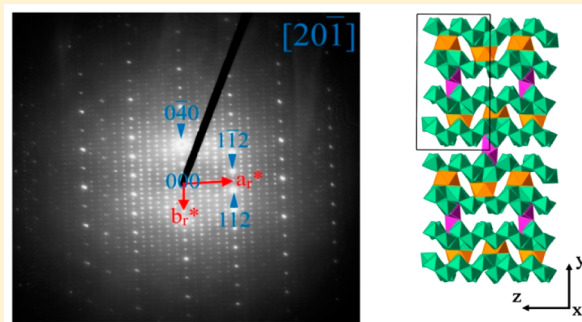
■ INTRODUCTION

Materials with oxygen hyperstoichiometry have recently gained importance in the field of solid oxide electrochemical cells due to their low activation energy for the motion of interstitial oxide ions, as, for example, in doped and undoped lanthanide silicate and germanate apatites,[1] melilites such as La$_{1+x}$Sr$_x$Ga$_3$O$_{7+x/2}$,[2,3] as well as oxides such as Ce(V,Ta)O$_{4+\delta}$.[4−7] Interstitial ion transport offers an alternative conduction mechanism to the vacancy transport found in high-symmetry three-dimensional mixed ionic electronic conductors such as La$_{1−x}$Sr$_x$(Co,Mn,Fe)-O$_{3−\delta}$ perovskite[8] and the ionic Zr$_{1−x}$Y$_x$O$_{2−\delta}$ fluorite materials[9] and could overcome the perceived requirement for high symmetry in new ion conducting materials. One of the early attempts to depart from vacancy-based transport was the development of the interstitialcy mechanism, as reported for the mixed conducting (La,Pr)$_2$(Ni,Co)O$_{4+\delta}$ Ruddlesden–Popper phases.[10,11] One of the more promising prototypical materials currently under investigation is low-symmetry [Ce$^{3+}_{1−2\delta}$Ce$^{4+}_{2\delta}$]NbO$_{4+\delta}$, which is a mixed ionic and p-type electronic conductor at oxygen chemical potentials close to

atmospheric (total conductivity, σ_{total} = 0.030 S cm^{-1} at 850 °C; ion transference number = 0.4; diffusion coefficient, D = 8.3 × 10^{-8} cm^2 s^{-1}).[12−16] The oxygen diffusivity is higher than the common electronic conductor La$_{1−x}$Sr$_x$MnO$_{3−\delta}$ and comparable with the mixed-conducting La$_{1−x}$Sr$_x$CoO$_{3−\delta}$ analogue despite possessing a slightly higher activation energy.[8,15] At ambient temperature four different crystal structures with varying oxygen contents have been identified in this family of materials corresponding to the formulas CeNbO$_4$, CeNbO$_{4.08}$, CeNbO$_{4.25}$, and CeNbO$_{4.33}$.[17,18] In order to better understand the oxygen transport mechanism and optimize performance, defect crystallography needs to be fully explored. The parent structure CeNbO$_4$, which does not contain any interstitial ions, was shown by powder neutron diffraction data to be a monoclinic fergusonite-type structure at room temperature[19,20] that transforms to a stoichiometric tetragonal polymorph (Scheelite type) at ≥800 °C.[15] We recently redetermined the structure of

CeNbO$_4$ from single-crystal X-ray diffraction,[20] while to date none of the hyperstoichiometric phases showing higher ionic conductivity than the stoichiometric $\delta = 0$ phases have solved crystal structures.[21,22] However, electron microscopy studies found alternating commensurate and incommensurate modulated structures,[16] which arise from the incorporation of excess oxygen on interstitial sites. In these cases charge balance is maintained by oxidation of Ce^{3+} to Ce^{4+}.[12,14,23] All previous structural refinements have used powdered samples; however, the Rietveld refinement of powder X-ray diffraction data for modulated structures with large cells or incommensuration is challenging and can lead to unconvincing refinements and/or ambiguous results. This is due to the large number of calculated reflections, high reflection overlap, and often weak supercell or incommensurate reflections. In order to minimize these issues, large single crystals of the parent structure were prepared, and subsequent post heat treatment of these crystals in appropriate oxidizing environments led to the formation of the $\delta > 0$ phases (Figure S1). The long-range average structure was modeled by analyzing the neutron and synchrotron X-ray powder diffraction data, and short-range coordination environment was determined using pair distribution function (PDF) analysis of neutron diffraction data obtained from powdered samples, prepared as outlined in our previous work.[20]

■ METHODS

Experimental. Commercial powders of CeO$_2$ (Merck, 99.9%) and Nb$_2$O$_5$ (Sigma Aldrich, 99.99%) were used as starting materials, mixed in stoichiometric proportions, and calcined in a box furnace at 1273 K in static air for 12 h. After grinding, the powder was pressed under an isostatic pressure of 100 MPa to prepare two cylindrical rods with an approximate diameter of 6 mm and a length of 40 mm, which were subsequently sintered at 1673 K for 16 h in air. The growth apparatus utilizes an optical floating zone furnace with four ellipsoidal mirrors in which 700 W halogen lamps were set as the infrared source with the growth rate of 10 mm/h, counter rotation rate of 40 rpm, and in flowing argon gas atmosphere. To prepare CeNbO$_{4.25}$ from the parent crystal CeNbO$_4$, a crystal with approximate dimensions $5 \times 5 \times 5$ mm was heated in a box furnace in static air at 873 K for 96 h and then quenched to room temperature. The phase purity of the parent and oxidized phases was confirmed using laboratory powder X-ray diffraction. The latter crystal was cleaved for analysis by single-crystal X-ray diffraction and collected at room temperature with a Bruker Smart Apex II three-circle diffractometer using graphite-monochromated Mo Kα radiation over $5° \leq 2\theta \leq 55°$. An empirical absorption correction was applied, and the data were refined using Jana 2006[24] utilizing the Superflip[25] structure solution algorithm. The atomic positions and anisotropic displacement parameters (ADPs) for Ce, Nb, and O were refined. Powders with the nominal composition of CeNbO$_{4.25}$ were analyzed using high-brilliance synchrotron radiation at I11 (Diamond Light Source, Rutherford Appleton Laboratory, Didcot, U.K., $\lambda = 0.826471$Å). The crystallographic model used was that derived from the single-crystal XRD data. Chebyshev polynomial coefficients, scale, lattice parameters, and spherical harmonics anisotropic peak broadening were sequentially refined using TOPAS V4.1.[26] Isotropic atomic displacement parameters were refined in groups for Ce, Nb, and O with the atomic fractional coordinate fixed. Neutron powder diffraction was conducted at the D2B beamline (Institut Laue-Langevin, Grenoble, France) using a wavelength of 1.594 Å. The same model as that used for the synchrotron powder XRD was used to fit the neutron powder diffraction data, and the same strategy used to refine the synchrotron powder XRD was applied, excluding the spherical harmonics anisotropic peak broadening factor. Total scattering neutron powder diffraction data were collected from the Polaris beamline at ISIS, Rutherford Appleton Laboratory, U.K., up to a value of 29.5 Å^{-1} in the scattering vector $Q = 4\pi \sin\theta/\lambda$. Background data from the instrument and sample holder were also collected and subtracted. The neutron diffraction data for Bragg scattering were

analyzed using GSAS,[27] and the total scattering data correction was performed using Gudrun[28] before the Reverse Monte Carlo[29,30] analysis adopted in RMCProfile.[31] For the CeNbO$_4$ data the model was based on a $10 \times 10 \times 10$ supercell (24000 atoms) based on the published structure,[19] while for the CeNbO$_{4.25}$ a $4 \times 4 \times 4$ supercell, using the structure derived in this work, was selected ensuring an ensemble of 19 200 atoms were included. Powders for electron diffraction were prepared by grinding under ethanol and drops of the resulting suspension deposited on lacey-carbon coated copper grids. Images were collected using a 200 kV JEOL-2100F microscope with a low-background Gatan double-tilt holder. Field-limiting apertures for selected-area electron diffraction (SAED) were 5, 20, and 60 μm in diameter. Crystals were tilted to $[010]$ and $[20\bar{1}]$ zone axes. High-resolution images were collected using an objective aperture (100 μm), corresponding to a nominal point-to-point resolution of $\sim$1.7 Å. Electron diffraction patterns were calibrated against external standards to derive reliable values for both the electron wavelength and the camera length. Lattice parameters were determined repeatedly to check for hysteresis of the electromagnetic lenses leading to errors $< \pm 1\%$.

Computational Methods. To study the diffusion dynamics of the oxygen ions in CeNbO$_4$ and CeNbO$_{4.25}$, molecular dynamics (MD) simulations based on a Born-like description[32] of the ionic lattices were performed. The interactions between ions were represented by long-range Coulombic force (summed using Ewald's method[33]) and the short-range Buckingham pair potential.[34] The cutoff distance for the summation of the Buckingham pair potential was 10.5 Å, as it is significant only at short range. The lattice energy is then given by

$$E_{\text{lattice}} = \sum_{j>i} \sum \left[\frac{q_i q_j}{4\pi\varepsilon_0 r_{ij}} + A_{ij}\exp\left(-\frac{r_{ij}}{\rho_{ij}}\right) - \left(\frac{C_{ij}}{r_{ij}^6}\right) \right]$$

where r_{ij} is the distance between ion i and j, $q_{i(j)}$ is the charge of ion $i(j)$, A_{ij}, ρ_{ij}, and C_{ij} are the Buckingham pair potential parameters (listed in Table S4), and ε_0 is the permittivity of free space. The starting crystal geometries used in the simulations were based on our previous measured values for CeNbO$_4$[20] and this work for CeNbO$_{4.25}$. The supercells used to construct the periodic lattices were of $10 \times 10 \times 8$ and $4 \times 4 \times 4$ unit cells for CeNbO$_4$ and CeNbO$_{4.25}$, respectively, with periodic boundary conditions applied. Both supercells contained 19 200 ions. All molecular dynamics simulations were performed using the DL_POLY4 package[35,36] with the velocity Verlet integration algorithm.[37] The oxygen diffusion behavior was studied in the temperature range of 573−2173K. The lattices were first relaxed using GULP (General Utility Lattice Program).[38] The relaxed supercell was equilibrated at constant volume (NVT) for 10 ps and then re-equilibrated at constant pressure (NPT), again for 10 ps. The lattice energies, volumes, and temperatures were checked to ensure equilibrium was reached. Diffusion dynamics data were collected for $\sim$100 ps using the Nosé−Hoover thermostat. The visual molecular dynamics (VMD) package was used to analyze the data.[39] The production run for this work was undertaken in NVT ensemble. The first 60 ps of data have been excluded from analysis to ensure equilibrium was reached. Table S5 lists the calculated lattice parameters for both systems showing good agreement with the experimentally measured lattice parameters.

■ RESULTS AND DISCUSSION

The selected area electron diffraction (SAED) pattern of single-crystal CeNbO$_{4.25}$, obtained from oxidizing CeNbO$_4$, shows a commensurately modulated phase compared to the parent phase (Figure 1). Along the $[010]_p$ zone axis (Figure 1a), the resultant superstructure reciprocal space unit cell was determined to be

$$\mathbf{a}_r^* = \frac{1}{12}[204]_P^*$$
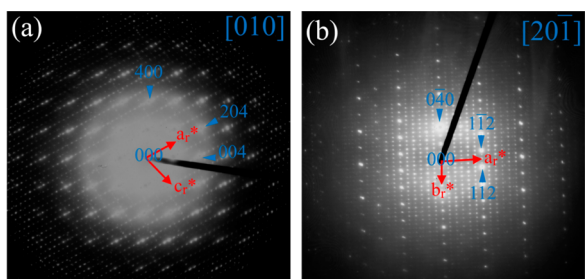
$$\mathbf{c}_r^* = \frac{1}{6}[\bar{2}02]_P^*$$

Figure 1. Selected area electron diffraction (SAED) of a $CeNbO_{4.25}$ crystal oriented along (a) $[010]_p$ and (b) $[20\bar{1}]_p$ showing a superstructure in $P2_1/c$ with the reciprocal space axes marked by red arrows. All indices are with respect to the parent substructure of $CeNbO_4$ crystallized in $I2/a$.

where p and r represent the parent and resultant superstructure cell, respectively.

In addition, to determining the unique $\mathbf{b}_r^*$, the crystal was oriented perpendicular to the first zone axis along $[20\bar{1}]_p$ zone axis, and it was concluded that $\mathbf{b}_r^* = (1/4)[020]_r^*$ (Figure 1b) resulted in the space group $P2_1/c$ as suggested previously.[16] Closer inspection of Figure 1b shows weak diffuse streaking along $\mathbf{a}_r^*$ consistent with stacking disorder. Hence, the resultant supercell real space unit cell derived from the observed reciprocal space is given by a matrix

$$\begin{pmatrix} \mathbf{a}_r \\ \mathbf{b}_r \\ \mathbf{c}_r \end{pmatrix} = \begin{pmatrix} 2 & 0 & 2 \\ 0 & 2 & 0 \\ -2 & 0 & 1 \end{pmatrix} \begin{pmatrix} \mathbf{a}_p \\ \mathbf{b}_p \\ \mathbf{c}_p \end{pmatrix}$$

The single-crystal X-ray diffraction reflections yielded a monoclinic cell (space group $P12_1/c1$; $a = 14.3732(8)$ Å, $b = 22.7921(12)$ Å, $c = 11.8319(6)$ Å, and $\beta = 105.071(2)°$, Table S1) in good agreement with the cell previously determined by Thompson et al.[16] using TEM ($P12_1/c1$ $a = 14.371(2)$ Å, $b = 22.748(6)$ Å, $c = 11.820(2)$ Å, and $\beta = 74.91(2)°$ where β is defined as the supplementary angle. Using 48 formula units per unit cell ($Z = 48$) 12 unique Ce and 12 unique Nb positions were readily found, while 51 unique oxygen sites were determined from the difference Fourier maps calculated using the Jana2006 software package[24] with the reliability indicators converging to acceptable values: $R = 0.0431$, $R_w = 0.0945$, $GOF = 1.79$ (Table S2). In addition, bond distances and angles fall within the expected ranges for ionic interactions, confirming a high-quality model.

Bond valence sums (BVS)[40,41] which measure the "bond strength" in ionic compounds using all interactions up to a distance of 3 Å are shown in Table S3. Different valence states of the Ce ions were distinguished from the BVS analysis. As expected from charge balance considerations in $CeNbO_{4.25}$, of the 12 unique Ce positions identified, six sites were found to contain Ce^{3+} and the remaining six were found to be Ce^{4+} sites. In the parent material, $CeNbO_4$, all of the Ce^{3+} ions are coordinated to 8 oxygen ions as first nearest neighbor and all of the Nb^{5+} ions are coordinated to 4 and 2 oxygen ions as first and second nearest neighbors, respectively; in $CeNbO_{4.25}$ the excess 0.25 oxygen per formula unit, equivalent to 12 extra oxygen ions in 3 unique Wyckoff sites, is expected to change the overall coordination environments of both ions significantly. From analysis of the BVS, on average Ce^{4+} ions were coordinated to fewer oxygen ions (8.67) when compared with Ce^{3+} (9.5) in $CeNbO_{4.25}$ and significantly more than the 8 coordinate environment in

stoichiometric $CeNbO_4$ within a 3 Å window. The higher coordination number could be achieved by adjusting the various Ce–O bond lengths so that the correct bond valence sums are satisfied. The bond valence sums for all Nb ions are calculated to be close to 5+ with slight underbonding found for one Nb equivalent position. The Nb ions retain their 6-coordinate environment with the exception of sites labeled as Nb(1) and Nb(8) (refer to SI), which enlarge to 8 and 7 coordinate, respectively, resulting in an average of $NbO_{6.25}$ for the first two nearest neighbor shells. This weakens oxygen binding energy to the niobium, allowing mobile oxygen to migrate from one crystallographic site to another.

Figure S2 compares the parent $CeNbO_4$ and oxidized $CeNbO_{4.25}$ projected along the principal axes of $[100]$, $[010]$, $[001]$, and $[101]$. Displacement of oxygen from the original positions in the parent structure on the xz plane is observed. In order to simplify the structural representation, in $CeNbO_4$, NbO_6 polyhedra are continuously connected by edge sharing in the xz plane with stacking along the y axis, creating a layered slab, while the incorporation of interstitial oxygen ions in $CeNbO_{4.25}$ is clearly positioned by the cooperative displacement mechanism of the surrounding oxygen ions to satisfy the bond valence sum (Figure 2a and 2b). Despite increasing the coordination number
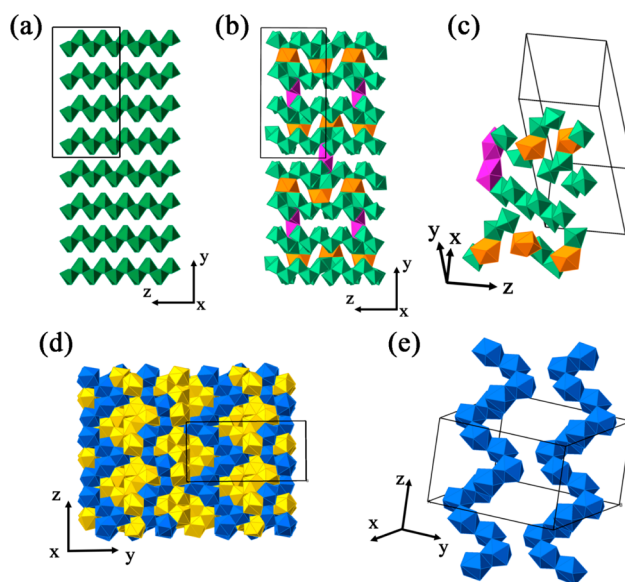

Figure 2. Structural arrangement of NbO_6 (green), NbO_7 (purple), and NbO_8 (orange) projected along $[100]$ in (a) $CeNbO_4$ and (b) $CeNbO_{4.25}$, while (c) illustrates connectivity between NbO_x slabs in the oxidized $CeNbO_{4.25}$ along y built by the insertion of interstitial oxygen ions creating edge-shared NbO_6–NbO_7–NbO_7–NbO_6, corner-connected NbO_6–NbO_8 (orange) and edge-shared NbO_8–NbO_6 polyhedra facilitating the improved conductivity. (d) Structural arrangement of $Ce^{4+}O_x$ (blue) and $Ce^{3+}O_x$ (yellow) polyhedra in $CeNbO_{4.25}$ projected along the principal $[100]$ and (e) $[−1.5, −0.7, −0.7]$. Ce^{4+} polyhedra are edge shared to form the continuous helical network along z.

of 6 for Nb ions to 7 giving $Nb(8)O_7$ and 8 giving $Nb(1)O_8$, the interstitial species are not located at the vacant $4b$ Wyckoff site in the distorted superstructure of the fluorite type[42,43] as suggested previously by Thompson et al.[16] (Figure S3). In between the NbO_6 slabs along the y axis the connectivity is built from sinusoidal bridging oxygens (Figure 2c), which is believed to facilitate enhanced ionic conductivity along the xz plane
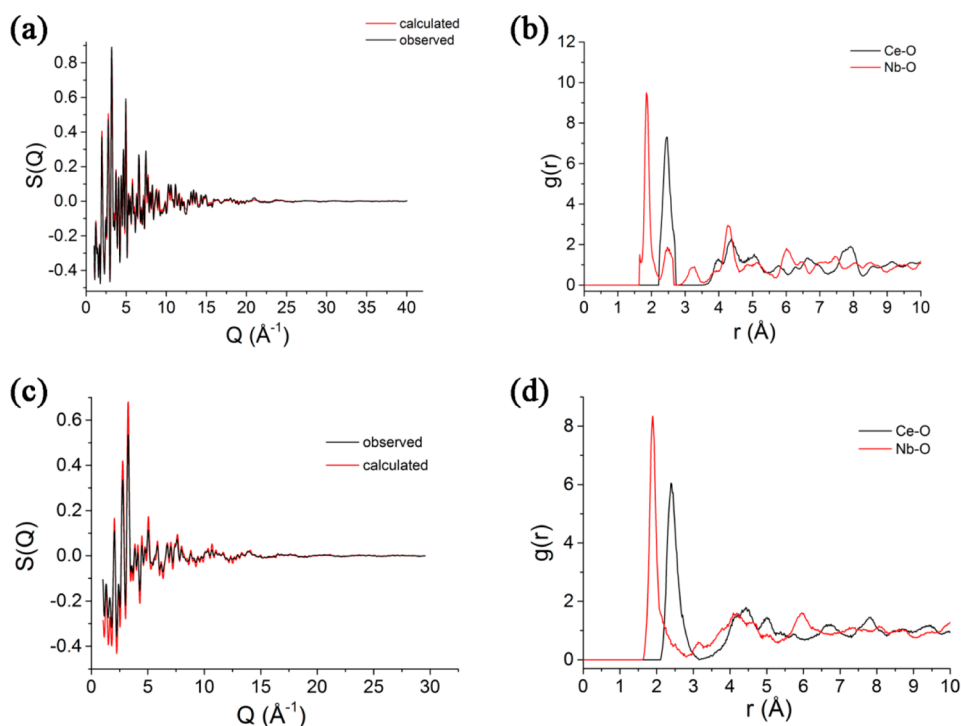
Figure 3. Pair distribution function analysis of $CeNbO_{4+\delta}$ powders showing (a) total scattering structure factor $S(Q)$ and (b) partial pair correlation functions $g(r)$ of $CeNbO_4$ and (c) $S(Q)$ and (d) $g(r)$ of $CeNbO_{4.25}$. For both cases Ce–O and Nb–O correlations were limited to $r \leq 10$ Å.

whenever the mobile oxygen ions encounter a hindrance along the slab and alternatively conduct to the next layer perpendicular (y direction) to the slabs, similar to the intertunnel diffusion found in the apatite electrolytes in addition to the major intratunnel migration.[44] Figure 2d and 2e shows solely the polyhedra of $Ce^{4+}O_x$ (blue) and $Ce^{3+}O_x$ (yellow) where the higher oxidation state Ce^{4+} species are found to form a continuous helical network running parallel to the crystallographic z axis, connected by edge sharing. In order to verify the average crystal structure of the powders, a Rietveld plot of synchrotron powder XRD and neutron diffraction patterns are presented in Figure S4, showing a good fit using the model derived from the single-crystal XRD data. R_{wp}, R_{Bragg}, and χ^2 for the synchrotron XRD and neutron diffraction Rietveld fits were 0.097, 0.035, and 1.28 and 0.034, 0.014, and 0.75, respectively.

In order to highlight differences in the local structure of the Ce and Nb environments, pair distribution function analysis of $CeNbO_4$ and $CeNbO_{4.25}$ powders was performed with the reliability factors for the Bragg profile fits being 0.046 and 0.044, respectively. The total scattering structure factor $S(Q)$ and partial pair correlation functions $g(r)$ of Ce–O and Nb–O with $r \leq 10$ Å are presented in Figure 3. The $g(r)_{Nb–O}$ of $CeNbO_4$ shows a separation between the first three coordination environments, while the shoulder at $2 \leq r \leq 3$ Å in the oxidized sample is consistent with the extended coordination of Nb–O from 6 to 7 and 8 due to the insertion of three interstitial oxygen ions per formula unit. The Ce–O pair correlation function in the latter sample is also broader, suggesting that the existence of mixed Ce^{3+} and Ce^{4+} ions must be facilitated by flexing the bond strength around the oxygen ion neighbors. The PDF histograms of the calculated Ce–O and Nb–O bond lengths are consistent with the data extracted from single-crystal X-ray diffraction (Figure 4). The close agreement between the structure obtained from powder and single-crystal diffraction (long range) supported by the short-range coordination information yielded

from the powder total scattering validates the usefulness of the "average" technique should the single crystal be difficult to produce.

To confirm that the helical Ce^{3+}/Ce^{4+} chains were favorable toward ion transport a molecular dynamics approach was employed. Initial lattice relaxation and optimization shows that better agreement between the experimental and the calculated lattice parameters of $CeNbO_{4.25}$ was achieved compared to the parent phase of $CeNbO_4$[20] with the same set of ionic potentials used. This suggests that the latter may not be a pure stoichiometric material but rather a slightly oxidized phase, while the former describes the positions of interstitial oxygens and the distinctive arrangement of Ce^{3+} and Ce^{4+} lattice sites. Figure 5 highlights the trajectory projections along the [010] and off-axis [001] directions, showing the mean square displacement (MSD) of ions after 100 ps. The $CeNbO_{4.25}$ sample clearly shows greater MSDs at 1073 K, indicating that the oxygen ions were mobile along the NbO_x polyhedra slab. An enlarged trajectory plot calculated at the high temperature of 1573 K is shown in Figure 5g, clearly showing that the major migration pathway lies in the xz plane but with some connectivity observed along the y crystallographic axis.

Figure 6a and 6b compares the MSD of oxygen in $CeNbO_{4.25}$ and $CeNbO_4$ at different temperatures. The parent phase does not show diffusion within the time frame used, while the oxidized phase readily allows diffusion. In an N ion system, the diffusivity is given by

$$\frac{1}{N} \sum_{i=1}^{N} [r_i(t) - r_i(0)]^2 = 6Dt + B$$

where $r_i(t) - r_i(0)$ is the displacement of an ion from its initial position after a time t, D is the ionic diffusion coefficient, t is time, and B is the displacement associated with the thermal vibrations around the equilibrium position.
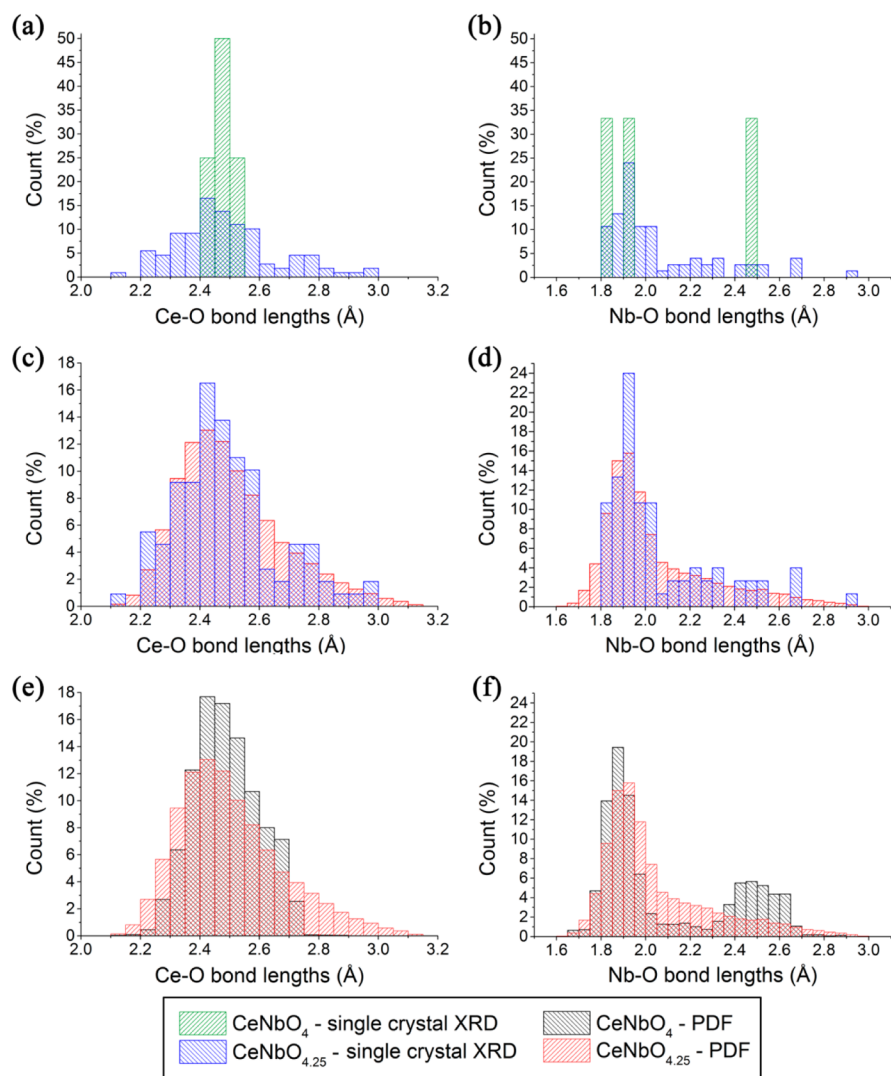
Figure 4. (a) Ce−O and (b) Nb−O bond length histogram of parent CeNbO$_4$[20] (green) and oxidized CeNbO$_{4.25}$ (blue) derived from single-crystal XRD showing a clear dispersion of the latter phase with the centroid located close to the parent phase. Total numbers of bond lengths for Ce−O in CeNbO$_4$ and CeNbO$_{4.25}$ are 8 and 109, and Nb−O are 6 and 75, respectively. (c) Ce−O and (d) Nb−O bond lengths histogram of CeNbO$_{4.25}$ derived from single-crystal XRD (blue) and PDF (red) with 27 809 Ce−O bonds and 19 105 Nb−O bonds for CeNbO$_{4.25}$-PDF; (e) Ce−O and (f) Nb−O bond lengths histogram of CeNbO$_4$ (black) and CeNbO$_{4.25}$ (red) derived from PDF with 32 000 Ce−O bonds and 24 053 Nb−O bonds for CeNbO$_4$-PDF.
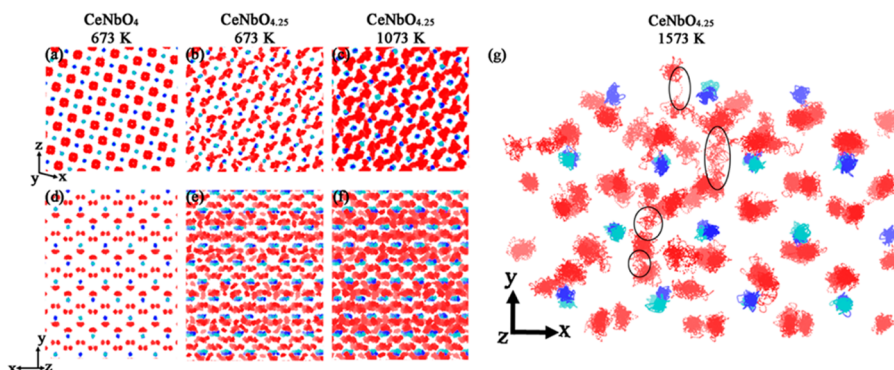

Figure 5. (a−c) [010] and (d−f) ∼[001] rotated 18° around y trajectory projections after 100 ps MD simulation: (a, d) CeNbO$_4$ at 673 K, (b, e) CeNbO$_{4.25}$ at 673 K, and (c, f) CeNbO$_{4.25}$ at 1073 K where light blue, dark blue, and red represent Ce$^{3+/4+}$, Nb^{5+}, and O$^{2−}$ ions, respectively. (g) Enlarged trajectory at 1573 K clearly showing the connectivity along the xz plane with the y migration additionally observed and highlighted.

The calculated diffusion coefficients at 1073, 1573, and 2173 K were 3×10^{-10}, 4×10^{-7}, and 3×10^{-6} cm^2 s^{-1}, respectively, with corresponding activation energies (E_a) of 1.10 (1373 K $\leq T \leq$ 2173 K) and 0.86 eV (1073 K $\leq T \leq$ 1173 K) (Figure 6c). At 1173 K the experimental value for D[14] is about 2 orders of magnitude lower than our computed value, with E_a 0.45 eV

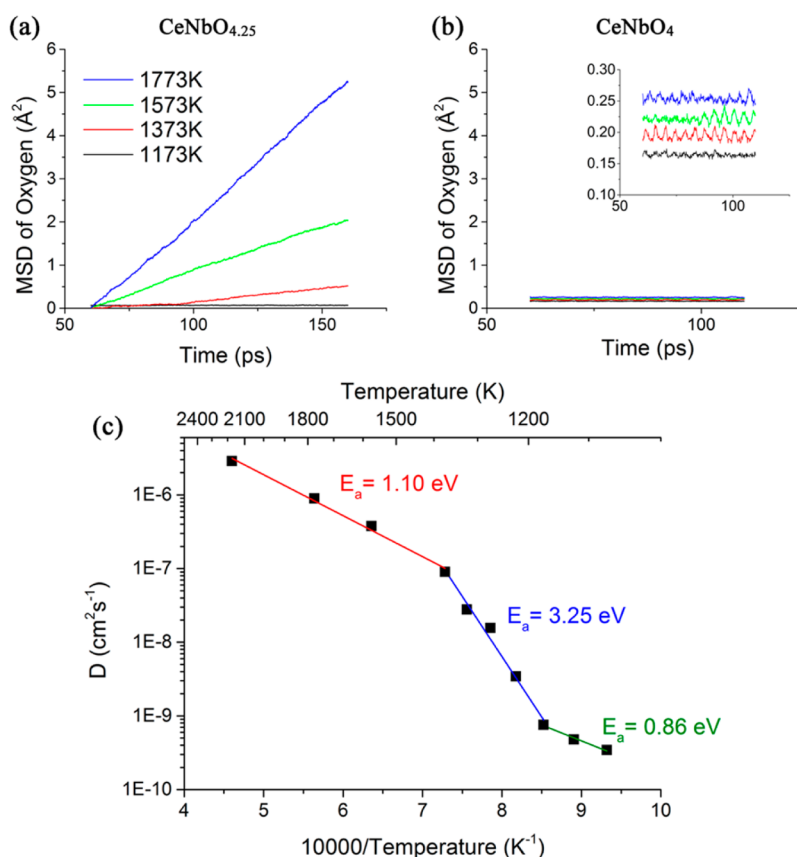**Figure 6.** Mean square displacement of oxygen of (a) $CeNbO_{4.25}$ and (b) $CeNbO_4$ at different temperatures showing that the parent phase does not diffuse within the time frame used while the oxidized phase readily diffuses. (c) Oxygen diffusivity showing regions with different calculated activation energies.

lower. However, a higher value for E_a of 0.99 eV was reported by Packer and Skinner,[15] which is comparable to this work. The difference in the activation energies may be associated with the transformation of the structure from commensurate oxygen excess $CeNbO_{4.25}$ at low temperatures to the high-temperature oxygen stoichiometric $CeNbO_4$ phase. It is well known that the lowest temperature accessed by the MD calculations is at the point at where the phase transition occurs and that the stoichiometric material is a poor oxygen ion conductor. This may also account for the difference in absolute oxygen diffusion coefficients. Another plausible explanation is that in the simulation the MSD was averaged over all oxygen ions which may underestimate the mobile ion in $CeNbO_{4.25}$.

CONCLUSIONS

Commensurately modulated $CeNbO_{4.25}$ with nominal oxygen excess has been shown to adopt a helical arrangement of $Ce^{3+}O_x$ and $Ce^{4+}O_x$ ($8 \leq x \leq 10$) using a combination of single-crystal and powder diffraction techniques, which leads to the anisotropic diffusion of oxygen along the xz slab. The interstitial oxygen extends the coordination of Nb from a nominal 6, within a 3 Å bond shell distance, to 7 and 8 that serves to increase the connectivity between the "NbO_6" layers. The local environment of the Nb−O and Ce−O pairs deduced from pair distribution function analysis confirms this average distorted coordination environment. This serves as an alternative pathway for the conducting oxygen to cross from one slab to another along the y direction whenever the oxide ion encounters a barrier, as seen in our molecular dynamics simulation at 1573 K, while the parent

$CeNbO_4$ phase remains nonconducting even at higher temperature. These observations on this complex crystal structure offer new insights in the development of high-performance materials for electrochemical devices, opening a wide compositional space that is no longer restricted to three-dimensional isotropic materials.

ASSOCIATED CONTENT

S Supporting Information

The Supporting Information is available free of charge on the ACS Publications website at DOI: 10.1021/jacs.5b11373.

Table of refined single-crystal X-ray diffraction data; table of refined atomic positions; table of selected bond lengths; table of Buckingham potentials; table of experimental and calculated lattice parameters; micrograph of the single crystal; model crystal structures; refined diffraction data; refined total scattering data; pair distributions correlations from MD; and associated references (PDF)
(CIF)

AUTHOR INFORMATION

Corresponding Authors
*tbaikie@ntu.edu.sg
*s.skinner@imperial.ac.uk
Present Address
△Department of Chemistry, University of Illinois at Chicago, 845 West Taylor Street (MC 111), Chicago, Illinois 60607, United States.

Notes

The authors declare no competing financial interest.

REFERENCES

(1) Orera, A.; Slater, P. R. *Chem. Mater.* **2010**, *22*, 675.
(2) Kuang, X.; Green, M. A.; Niu, H.; Zajdel, P.; Dickinson, C.; Claridge, J. B.; Jantsky, L.; Rosseinsky, M. J. *Nat. Mater.* **2008**, *7*, 498.
(3) Wei, F.; Gasparyan, H.; Keenan, P. J.; Gutmann, M.; Fang, Y.; Baikie, T.; Claridge, J. B.; Slater, P. R.; Kloc, C. L.; White, T. J. *J. Mater. Chem. A* **2015**, *3*, 3091.
(4) Packer, R. J.; Barlow, J.; Cott, A.; Skinner, S. J. *Solid State Ionics* **2008**, *179*, 1094.
(5) Skinner, S. J.; Palmer, H. M.; Raj, E. S.; Kilner, J. A. *J. Solid State Chem.* **2004**, *177*, 2685.
(6) Negas, T.; Roth, R. S.; McDaniel, C. L.; Parker, H. S.; Olson, C. D. *Mater. Res. Bull.* **1977**, *12*, 1161.
(7) Roth, R. S.; Negas, T.; Parker, H. S.; Minor, D. B.; Jones, C. *Mater. Res. Bull.* **1977**, *12*, 1173.
(8) Carter, S.; Selcuk, A.; Chater, R. J.; Kajda, J.; Kilner, J. A.; Steele, B. C. H. *Solid State Ionics* **1992**, *53–56*, 597.
(9) Minh, N. Q. *J. Am. Ceram. Soc.* **1993**, *76*, 563.
(10) Chroneos, A.; Yildiz, B.; Tarancon, A.; Parfitt, D.; Kilner, J. A. *Energy Environ. Sci.* **2011**, *4*, 2774.
(11) Kushima, A.; Parfitt, D.; Chroneos, A.; Yildiz, B.; Kilner, J. A.; Grimes, R. W. *Phys. Chem. Chem. Phys.* **2011**, *13*, 2242.
(12) Tsipis, E. V.; Munnings, C. N.; Kharton, V. V.; Skinner, S. J.; Frade, J. R. *Solid State Ionics* **2006**, *177*, 1015.
(13) Packer, R. J.; Skinner, S. J.; Yaremchenko, A. A.; Tsipis, E. V.; Kharton, V. V.; Patrakeev, M. V.; Bakhteeva, Y. A. *J. Mater. Chem.* **2006**, *16*, 3503.
(14) Packer, R. J.; Tsipis, E. V.; Munnings, C. N.; Kharton, V. V.; Skinner, S. J.; Frade, J. R. *Solid State Ionics* **2006**, *177*, 2059.
(15) Packer, R. J.; Skinner, S. J. *Adv. Mater.* **2010**, *22*, 1613.
(16) Thompson, J. G.; Withers, R. L.; Brink, F. J. *J. Solid State Chem.* **1999**, *143*, 122.
(17) Skinner, S. J.; Kang, Y. *Solid State Sci.* **2003**, *5*, 1475.
(18) Santoro, A.; Marezio, M.; Roth, R. S.; Minor, D. *J. Solid State Chem.* **1980**, *35*, 167.
(19) Skinner, S. J.; Brooks, I. J. E.; Munnings, C. N. *Acta Crystallogr., Sect. C: Cryst. Struct. Commun.* **2004**, *60*, I37.
(20) Bayliss, R. D.; Pramana, S. S.; An, T.; Wei, F.; Kloc, C. L.; White, A. J. P.; Skinner, S. J.; White, T. J.; Baikie, T. *J. Solid State Chem.* **2013**, *204*, 291.
(21) Cava, J. R.; Roth, R. S. *AIP Conf. Proc.* **1979**, *53*, 361.
(22) Cava, R. J.; Roth, R. S.; Negas, T.; Parker, H. S.; Minor, D. B. *J. Solid State Chem.* **1981**, *40*, 318.
(23) Skinner, S. J.; Packer, R. J.; Bayliss, R. D.; Illy, B.; Prestipino, C.; Ryan, M. P. *Solid State Ionics* **2011**, *192*, 659.
(24) Petříček, V.; Dušek, M.; Palatinus, L. *Z. Kristallogr. - Cryst. Mater.* **2014**, *229*, 345.
(25) Palatinus, L.; Chapuis, G. *J. Appl. Crystallogr.* **2007**, *40*, 786.
(26) *TOPAS V4.1*; Bruker AXS Inc.: Madison, WI, 2008.
(27) Larson, A. C.; Dreele, R. B. V. *General Structure Analysis System (GSAS)*; Los Alamos National Laboratory: Los Alamos, NM, 2004.
(28) Soper, A. K.; Barney, E. R. *J. Appl. Crystallogr.* **2011**, *44*, 714.
(29) McGreevy, R. L.; Pusztai, L. *Mol. Simul.* **1988**, *1*, 359.
(30) McGreevy, R. L. *Nucl. Instrum. Methods Phys. Res., Sect. A* **1995**, *354*, 1.
(31) Tucker, M. G.; Keen, D. A.; Dove, M. T.; Goodwin, A. L.; Hui, Q. *J. Phys.: Condens. Matter* **2007**, *19*, 335218.
(32) Born, M.; Mayer, J. E. *Eur. Phys. J. A* **1932**, *75*, 1.
(33) Ewald, P. *Ann. Phys.* **1921**, *369*, 253.
(34) Buckingham, R. A. *Proc. R. Soc. London, Ser. A* **1938**, *168*, 264.
(35) Smith, W.; Forester, T. R. *J. Mol. Graphics* **1996**, *14*, 136.
(36) Todorov, I. T.; Smith, W.; Trachenko, K.; Dove, M. T. *J. Mater. Chem.* **2006**, *16*, 1911.
(37) Swope, W. C.; Andersen, H. C.; Berens, P. H.; Wilson, K. R. *J. Chem. Phys.* **1982**, *76*, 637.
(38) Gale, J. D. *J. Chem. Soc., Faraday Trans.* **1997**, *93*, 629.
(39) Humphrey, W.; Dalke, A.; Schulten, K. *J. Mol. Graphics* **1996**, *14*, 33.
(40) Brese, N. E.; O'Keeffe, M. *Acta Crystallogr., Sect. B: Struct. Sci.* **1991**, *47*, 192.
(41) Brown, I. D.; Altermatt, D. *Acta Crystallogr., Sect. B: Struct. Sci.* **1985**, *41*, 244.
(42) Hahn, T.; Looijenga-Vos, A. In *International Table for Crystallography*; Hahn, T., Ed.; Springer: Heidelberg, 2006; Vol. A.
(43) Swanson, H. E.; Tatge, E. *Standard X-ray diffraction powder patterns*; National Bureau of Standards: Washington, DC, 1953.
(44) Pramana, S. S.; Klooster, W. T.; White, T. J. *Acta Crystallogr., Sect. B: Struct. Sci.* **2007**, *63*, 597.